47th AIAA Aerospace Sciences Meeting Including The New Horizons Forum and Aerospace Exposition
5 - 8 January 2009, Orlando, Florida

AIAA 2009-174

A Numerical Study of Purdue's Mach 6 Tunnel with a Roughness Element

Patrick T. Greene,* Jeff D. Eldredge, † Xiaolin Zhong ‡ and John Kim §
University of California, Los Angeles, CA, 90095-1597, USA

The effects of surface roughness on the stability of hypersonic flow are of great importance to hypersonic vehicles. The overall goal of our research is to provide a better understanding of the effects of surface roughness on transitional and turbulent hypersonic boundary layers. Direct numerical simulations have been performed of flow in the Boeing/AFOSR Mach 6 quiet wind tunnel at Purdue University. Three-dimensional simulations were performed of the nozzle without any roughness and 2D simulations were performed with an isolated roughness element located on the wall of the nozzle. Two different roughness heights were simulated, both of which were less then the local undisturbed boundary layer thickness. The roughness elements produced a combination of Mach wave and expansion fan in the nozzle. The influence of the roughness elements on the flow is investigated in this paper. It is found that the presence of the elements has a substantial effect on the boundary layer and stability profiles downstream of the element.

Nomenclature

$h(x)$	height of roughness element used in simulations
h_0	height of Purdue roughness element
M	Mach number
P	fluid pressure
r_0	radius of Purdue roughness element
T	fluid temperature
(U, V)	velocity components along horizontal and vertical directions
(x, y)	horizontal and vertical coordinates ($x = 0$ corresponds to the nozzle throat; $y = 0$ corresponds to center of nozzle)
x_r	x location of roughness element
δ	boundary layer thickness
ρ	fluid density

I. Introduction

The ability to accurately predict the location of laminar to turbulent transition is of great importance to the design of hypersonic vehicles. As the flow undergoes transition, there are large changes in heat transfer rates and skin friction drag.[1] Without the knowledge of the transition location, designers of hypersonic vehicles must be overly cautious with their designs. Thermal protection and propulsion systems must assume turbulent flow over the entire body. In spite of its importance, the mechanisms leading to transition of hypersonic boundary layers are still poorly understood.[2] Predicting the location of transition is further complicated by the presence of isolated roughness elements and distributed roughness. Isolated roughness elements can be found on many hypersonic vehicles. For example, the antenna on the Apollo

*Graduate Student, Department of Mechanical and Aerospace Engineering, greene@seas.ucla.edu, Student Member, AIAA.
†Assistant Professor, Department of Mechanical and Aerospace Engineering, Member, AIAA.
‡Professor, Department of Mechanical and Aerospace Engineering, Associate Fellow, AIAA.
§Professor, Department of Mechanical and Aerospace Engineering, Member, AIAA.

reentry capsule[3] and the tiled surface of the space shuttle when the largest local flaws are examined in detail.[2]

The e^n method, which is based on the normal-mode instability, cannot explain bypass transition such as roughness-induced nosetip transition in hypersonic boundary layers. Recent theoretical studies have shown the importance of transient growth and surface roughness in bypass transition.[4–7] Transient growth is a result of the coupling between oblique Orr-Sommerfeld and Squire modes, which leads to algebraic growth followed by exponential decay in the early region in the boundary layers. Reshotko and Tumin[6] developed a spatial theory of optimal disturbances in boundary layers. It was found that the most significant transient growth is associated with stationary streamwise vortices.

Reshotko and Tumin[7] proposed a transient-growth model for early transition due to distributed roughness by using computational results based on their spatial transient growth theory. Their transient growth based transition relations reproduce the trend of Reda and the passive nosetip technology (PANT) data.[8,9] The transient growth theory does not explain the receptivity of the optimal growth associated with stationary streamwise vortices. Instead, Reshotko and Tumin[7] assumed a linear wave growth with respect to the roughness height. The exact receptivity mechanisms, which are critical to the explanation of transition by the transient growth theory, are still not known. Recently, White et al.[10,11] have performed a series of experiments on transient growth of stationary disturbances in a flat plate incompressible boundary layer. Direct numerical simulations of Whites experiments have been carried out by Choudhari and Fischer.[12,13] Experimental results indicate that disturbances generated by surface roughness undergo suboptimal growth, which is significantly different from theoretical optimal growth. For hypersonic boundary layers, so far, there has not been any reported computational (or experimental) study on transient growth theory, its receptivity to surface roughness, and its nonlinear breakdown. Such computational simulations can be valuable to the development of a transient-growth model for bypass transition.

The objective of the current paper is to investigate the effects of an isolated roughness element on hypersonic flow. This goal is accomplished by numerically simulating flow within the Boeing/AFOSR Mach 6 quiet wind tunnel at Purdue University with an isolated roughness element located along the wall. The compressible Navier-Stokes equations are solved using a fifth-order WENO scheme and a TVD scheme for time advancement. Numerical simulations without a roughness element for two different stagnation pressures are presented as validation of the methodology used to model the Purdue nozzle. The complicated flow structure generated by the presence of an isolated roughness element in the nozzle is examined in the current paper.

II. Problem Statement

The geometry of interest is the Boeing/AFOSR Mach 6 wind tunnel at Purdue University. The wind tunnel at Purdue is a Ludwieg Tube capable of generating quiet Mach 6 flow and is maintained by Professor Steven Schneider.[15] By simulating flow in this tunnel, we are able to validate our data by comparing to the

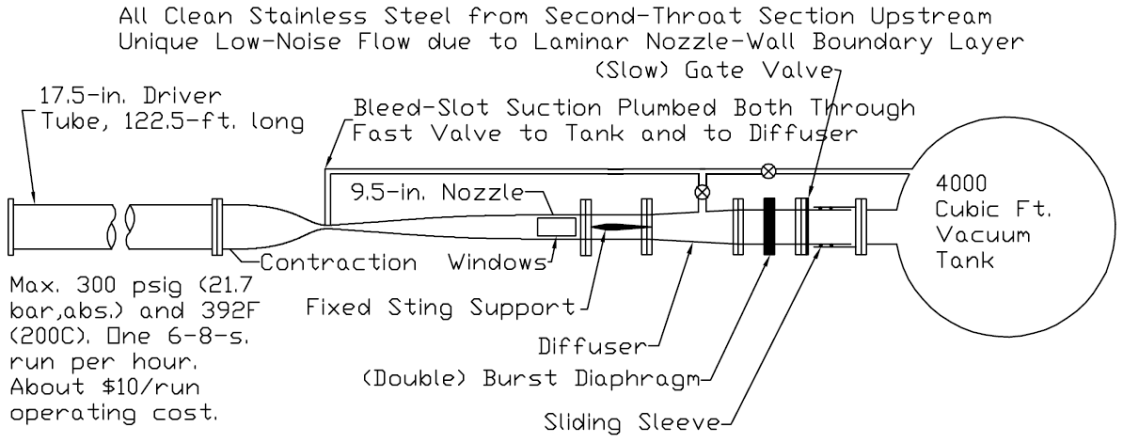

Figure 1. Boeing/AFOSR Mach 6 Wind Tunnel (figure from Borg et al.[14])

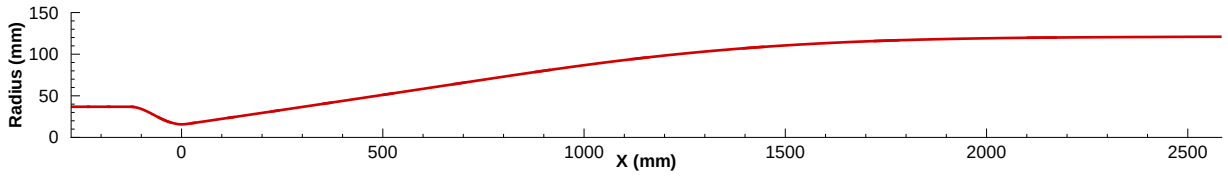

Figure 2. Portion of Boeing/AFOSR Mach 6 wind tunnel being simulated

experimental results obtain by Schneider and coworkers. A diagram of the Boeing/AFOSR Mach 6 wind tunnel is shown in Fig. 1. The wind tunnel consists of a long driver tube followed by a converging-diverging nozzle and the test section. The tunnel is approximately 40 m long from the driver tube to the test section. A majority of the length of the the total nozzle is the driver tube which is 37.3 m long. The nozzle utilizes a bleed just before the throat. The bleed restarts the boundary layer and helps ensure quiet flow in the test section of the nozzle.

The performed simulations are only concerned with a portion of the converging-diverging nozzle section, specifically, from a small portion of the converging section to the end of the test section. Simulating the bleed is also beyond the interest of the current study. The bleed is modeled using different boundary conditions along the wall as explained in section III. The section of the nozzle used in the simulations to obtain the undisturbed flow without the roughness element (or base flow) is shown in Fig. 2. The converging section is an arbitrary addition that does not match the Purdue geometry. A straight portion was added upstream of the converging section.

Experiments with an isolated roughness element are currently being performed at Purdue University. Preliminary results from these experiments have been provided by Schneider (personal communication). The roughness element used was a micrometer head with a diameter of 5.969 mm and a height varying from 2.54 mm to 19.304 mm. The roughness element is located 1.924 m from the throat of the nozzle. At the location of the roughness element, the boundary layer thickness is approximately 8 mm for a stagnation pressure of 900 kPa (130 psia) when the roughness element is not present. Since a body fitted grid is being employed in the numerical simulations, the current simulations use a smooth roughness element instead of a micrometer head. The height of the smooth roughness element is a Gaussian given by $h(x) = h_0 \exp\left(-\left(\frac{x-x_r}{r_0}\right)^2\right)$, where h_0 is the roughness height, x_r is the x position of the roughness element and r_0 is the radius of the roughness element. A comparison between the micrometer used at Purdue University set to 6.604 mm and the smooth roughness element used in the simulations is shown in Fig. 3.

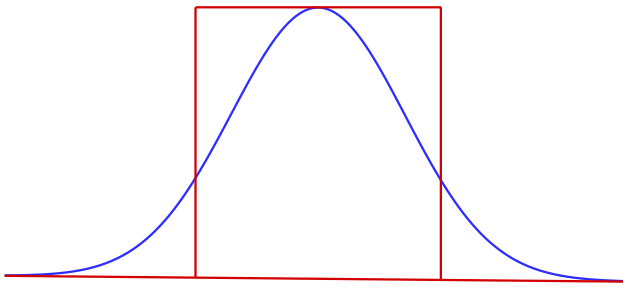

Figure 3. Comparison between 6.604 mm Purdue roughness element and smooth roughness element. Purdue roughness element ——; Smooth roughness element used in simulation ——.

III. Methodology

Direct numerical simulation (DNS) of the compressible Navier-Stokes, continuity and energy equations in conservative form on a curvilinear grid are performed to compute the flow field inside the nozzle. The air in the nozzle is assumed to be a perfect gas. The dynamic viscosity is calculated using Sutherland's formula and Stokes' assumption is used to relate the dynamic viscosity and second viscosity coefficient.

Two different numerical methods were used to simulate the flow in the nozzle: one method for when the roughness was not present and another for when it was present. For flow without the roughness element, an explicit third-order upwinding finite difference scheme was used.[16] Since the nozzle is axisymmetric when the roughness element is not present, Fourier collocation was used to compute any derivatives in the azimuthal direction. A third-order low-storage Runge-Kutta scheme[17] was used for time advancement and fourth-order central finite differencing was used to compute the viscous fluxes. For the flow with the roughness element, flow discontinuities such as shocks may be present, so a WENO shock-capturing scheme with Roe

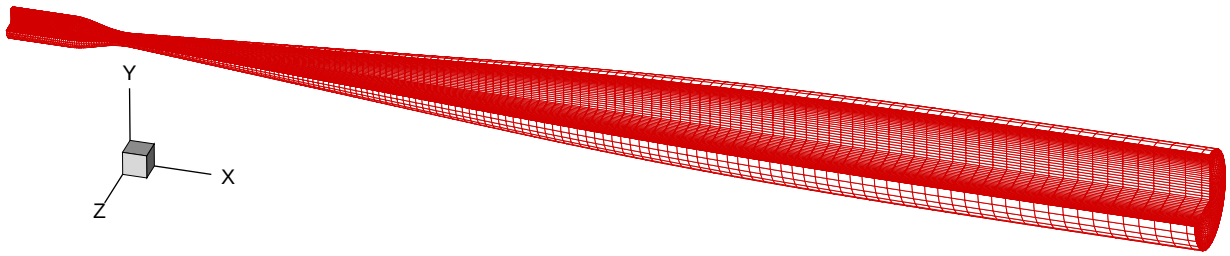

Figure 4. Example of grid for flow without roughness element

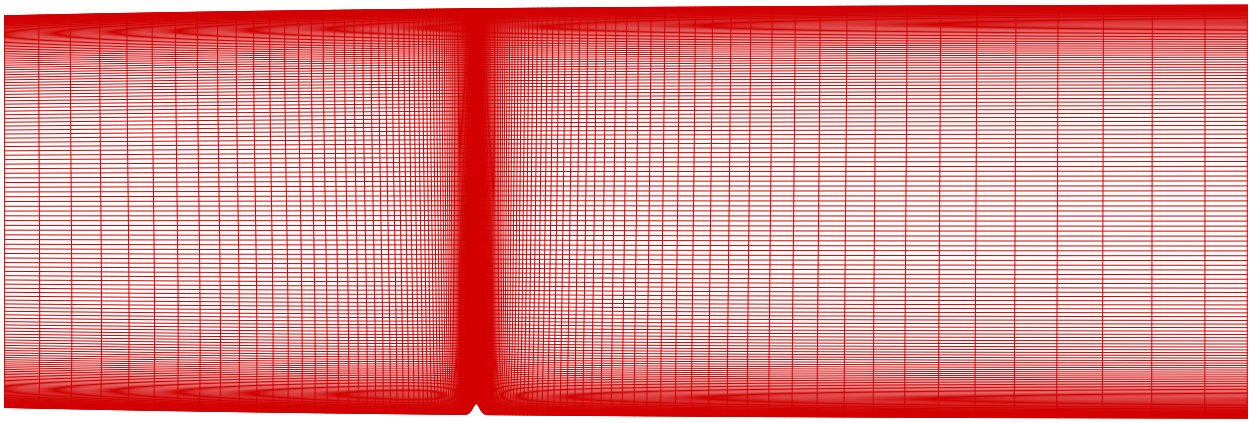

Figure 5. Grid for flow with 6.60 mm roughness element. Only every fourth point is shown.

flux splitting was used to compute the inviscid fluxes.[18] A third-order TVD[18] (total variation diminishing) scheme was used for time advancement and the viscous fluxes were computed using sixth-order central finite differencing. Thus far only 2D simulations have been performed with the roughness element.

The grid for flow without a roughness element begins 0.27 m upstream of the throat of the nozzle and ends 2.58 m downstream the throat. A sample grid is shown in Fig. 4, where the flow goes from left to right. The converging section of the nozzle is an arbitrary addition that does not match the Purdue geometry. The converging section of the Purdue nozzle opens to the driver tube where the flow velocity is nearly zero. If the converging section in the simulations matched the Purdue geometry, the simulations would take an unacceptable amount of time to converge due to the low inlet velocity. A straight portion was added before the converging section to allow parallel inflow conditions. The shape of the simulated nozzle matches the Purdue geometry from the location of the bleed in the Purdue nozzle to the outlet of the computational grid. In the computations, the bleed was simulated through the use of different boundary conditions along the wall as discussed later in the current section. The grid is algebraically generated with clustering near the walls and inlet. The clustering near the walls is present to resolve the thin boundary layer that is created. The clustering near the inlet assists in the capture of the 'leading edge' after the simulated bleed and the rapid change in flow properties at the throat. The number of grid points used varied from 200 in the streamwise direction by 100 in the radial to 800 in the streamwise by 800 in the radial. Since Fourier collocation was used in the azimuthal direction, only four points were used in the azimuthal direction.

The 2D grid with the roughness element begins 1.65 m downstream of the throat of the nozzle and ends 2.37 m downstream of the throat. An elliptic grid generation method[19] was used to generate the grid. The grid is a body fitted grid around a smooth isolated roughness element with orthogonality imposed along the lower wall with the roughness element. The grid for a 6.60 mm roughness element is shown in Fig. 5 where the flow goes from left to right. An enlarged view of the grid in the vicinity of the roughness element is shown in Fig. 6. As in the grid without the roughness element, this grid also has clustering near the walls. However, there is now clustering around the roughness element in the streamwise direction. This is done

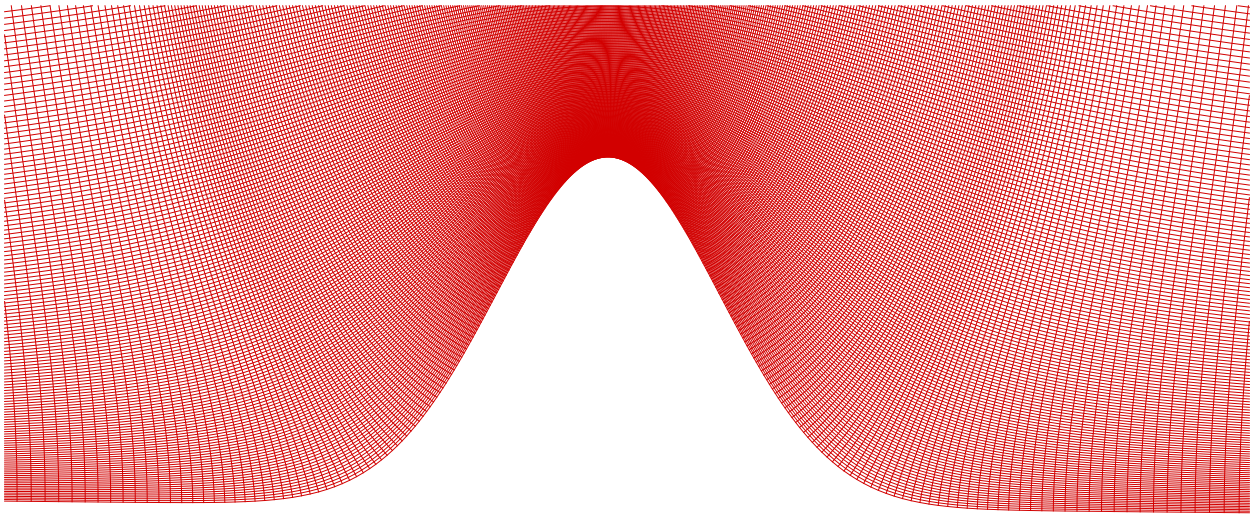

Figure 6. Grid in vicinity of 6.60 mm roughness element

to capture the complicated flow structure around the roughness element. The grids used in the simulations with the roughness elements both had 800×800 grid points.

The two simulations utilize different sets of boundary conditions. For the simulations without the roughness element, the wall boundary conditions need to simulate the bleed in the Purdue nozzle since the bleed is not being included in the numerical simulations. This is done because the bleed would require a significant increase in the number of grid points to accurately capture the flow around the bleed and would thus increase the required computational resources and time. Since the flow around the bleed is not the portion of interest in the current paper, increasing the grid points there was not a viable option. The bleed was therefore simulated by changing the wall boundary conditions at the location of the bleed. Upstream of the bleed, inviscid slip boundary conditions were used. The slip boundary conditions impose no flow through at the wall while extrapolating the tangential velocity from the interior of the domain. Downstream of the bleed, no slip boundary conditions are used. Figure 7 shows where the different boundary conditions are applied. Both portions have adiabatic walls.

A symmetry boundary condition is implemented on the conservative variables along the centerline of the nozzle. Since inviscid slip boundary conditions are being used on the walls at the inlet, inviscid characteristic boundary conditions[20] are applied there. At the inlet, the stagnation pressure and stagnation temperature are specified and the non-streamwise velocity components are set to zero. The inviscid characteristic equations are solved to calculate the streamwise velocity. From these, the isentropic relationships are use to calculate the static pressure and static temperature. At the outlet, the flow is mostly supersonic and therefore the conservative variables are extrapolated from the interior of the domain.

For the simulations with the roughness element, the boundary conditions on the wall are adiabatic and no slip everywhere. At the inlet, most of the flow is supersonic already so the conservative variables are interpolated from previous 2D simulations of the full nozzle without the roughness element. Just as in the case without the roughness element, the conservative variables at the outlet are extrapolated from the interior.

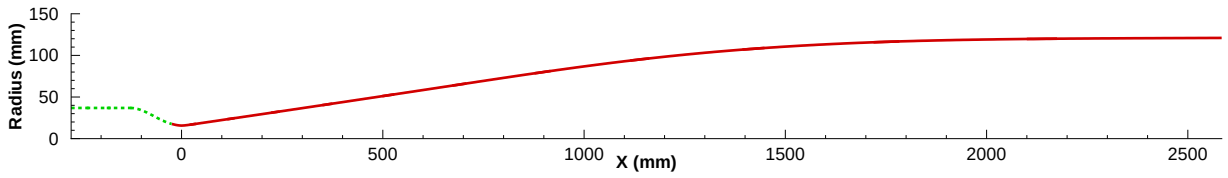

Figure 7. Wall boundary condition locations. Viscous, ——; Inviscid, - - -.

IV. 3D Base Flow Results

IV.A. Low Stagnation Pressure

Two different stagnation conditions were simulated without a roughness element as validation cases for the model of the wind tunnel. The first case has a stagnation pressure of 134.9 kPa (19.57 psia) and a stagnation temperature of 433 K. These values were chosen because a boundary layer profile for these conditions is provided by Skoch in his Ph.D. thesis.[21] In the thesis, Pitot tube measurements of the stagnation pressure are provided 1.912 m downstream of the throat of the nozzle. Using these measurements, a Mach number profile can be computed by assuming constant static pressure through the boundary layer. A comparison of the simulation results and the Mach profile calculated from the Skoch thesis is shown in Fig. 8.

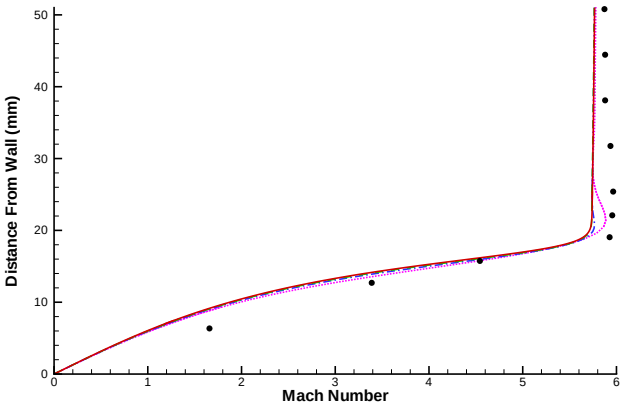

Figure 8. Mach profile for low stagnation pressure case. Values represent number of grid points in streamwise direction by radial direction. 200×200 ·····; 400×200 -·-; 400×400 - - -; 800×800 ——; Purdue results •.

As seen in the figure, the boundary layer profile converged with the 400×400 grid. An interesting feature can be found in the profile before grid convergence. If the grid is too coarse, the Mach number at the edge of the boundary layer overshoots the freestream Mach number, exhibiting a bump in the boundary layer profile. This is best seen in the 200×100 grid. As the grid is refined, the magnitude of the overshoot is decreased until the overshoot is removed.

The simulation results show good agreement with the experimental measurements. There is a discrepancy in the freestream Mach number, but this is most likely due to the bleed in the actual nozzle. Although the boundary conditions being used along the wall of the simulation allow the boundary layer to start at the same location, they don't simulate any changes to the stagnation conditions that the bleed may cause. These changes could result in the discrepancy seen in the Mach number.

IV.B. High Stagnation Pressure

The second validation case has a stagnation pressure of 896.3 kPa (130 psia) and stagnation temperature of 433 K. These stagnation conditions were chosen because Schneider provided a computed boundary layer profile from the boundary layer code used to design the Purdue wind tunnel. The profile is at a location 1.83 m from the nozzle throat. The computer code used by Schneider was the Sivells' nozzle design code. A comparison between the results from the design code and our simulations is shown in Fig. 9.

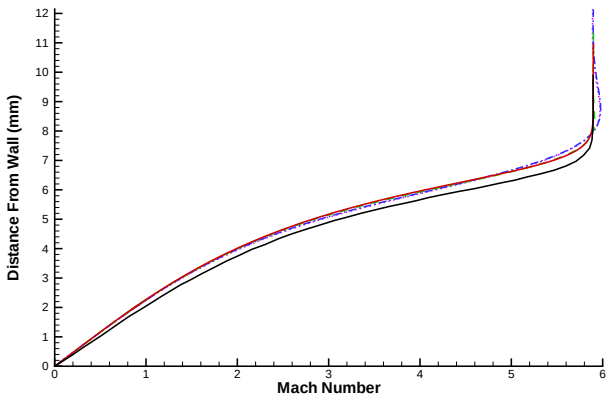

(a) Dimensional boundary layer. 400×200 ·····; 800×200 -·-; 800×400 - - -; 800×800 ——; Purdue computation ——.

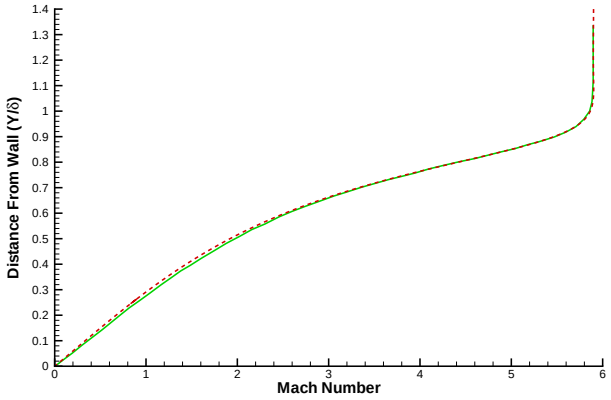

(b) Scaled profile from 800x800 grid. δ is the boundary layer height. Purdue computation ——; Simulation results - - -.

Figure 9. Mach profile for high stagnation pressure. Values represent number of grid points in streamwise direction by radial direction.

The boundary layer profile did not converge until the 800×400 grid was used. Figure 9(a) also shows the small overshoot of the Mach number at the end of the boundary layer as seen in the low stagnation pressure case. The figure also shows very little change in the profile when the streamwise grid points were increased from 400 to 800. Based on this, the 400×400 grid would probably have been sufficient to resolve the flow.

Figure 9(a) shows the comparison between the two Mach number profiles in dimensional wall-normal coordinates. There is a small difference in the boundary layer thickness, which can be due to two sources. The first is the Sivells' code, which is an inviscid code that use a laminar boundary layer displacement correction and therefore is not as accurate as DNS of the Navier-Stokes equations. The second source may be from a discrepancy in the location of the bleed between the Sivells' code and our simulations. If the location of the bleed is the source of the difference, then if the profiles are non-dimensionalized by the boundary layer thickness, the profiles should match, due to the self-similarity of the boundary layer. Figure 9(b) shows the same profiles non-dimensionalized by local boundary layer thickness. The non-dimensional boundary layer profile from the simulations and the Sivells' code match very well. Therefore the difference in boundary layer thickness is most likely due to a small difference in the effective location of the bleed.

In light of their relevance to stability, the first derivative of the velocity and the derivative of the density times the first velocity derivative were calculated at 1.83 m from the nozzle throat and are shown in Fig. 10. Both plots in Fig. 10 have very smooth and well resolved profiles. The temperature and its derivative are shown in Fig. 11.

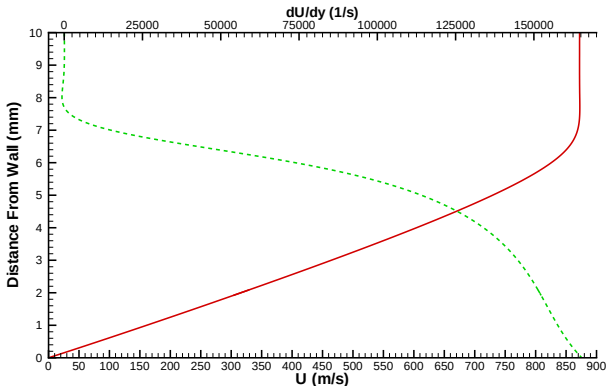

(a) First derivative of velocity. U ——; dU/dy - - -.

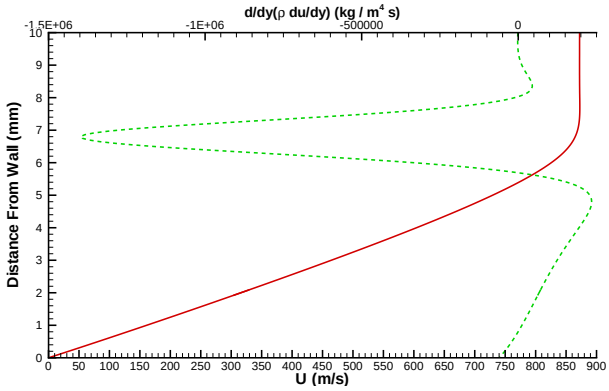

(b) Derivative of density times first derivative of velocity. U ——; $d/dy(\rho dU/dy)$ - - -.

Figure 10. Velocity profile with first and second derivatives for 130 psia stagnation pressure. From 800x800 grid.

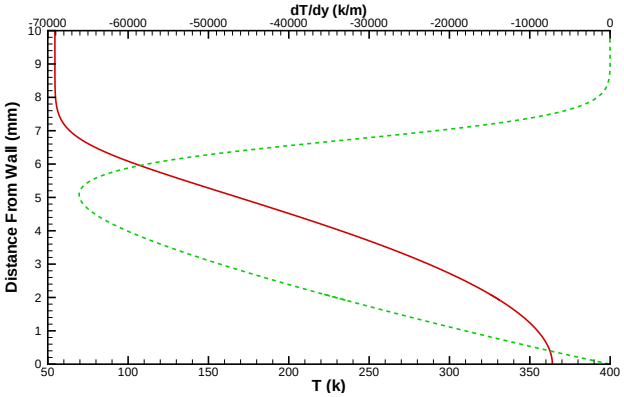

Figure 11. Temperature profile with first derivative for 130 psia stagnation pressure. From 800x800 grid. T ——; dT/dy - - -.

V. 2D Roughness Element Results

Two-dimensional simulations with two different roughness heights have been performed. The heights and shapes are provided in Fig. 12 along with a comparison to the Mach profile at the roughness location for flow without the roughness element. The smaller roughness element is the minimum height used in the roughness experiments being performed at Purdue. The taller element was chosen with future 3D simulations in mind. This height produces an interesting wall temperature contour as deminstrated in recent experiments with temperature sensitive paint (Schneider, personal communication). The Reynolds numbers based on the roughness height and the local conditions in the undisturbed laminar boundary layer profile at the roughness height are 980 for the short roughness element and 20,800 for the taller one. The simulations were both performed with a stagnation pressure of 134.9 kPa (19.57 psia) and a stagnation temperature of 433 K. These conditions result in a Mach number of approximately 3.6 at the center of the nozzle above the roughness element and a boundary layer thickness of approximately 10 mm if the roughness element is not present.

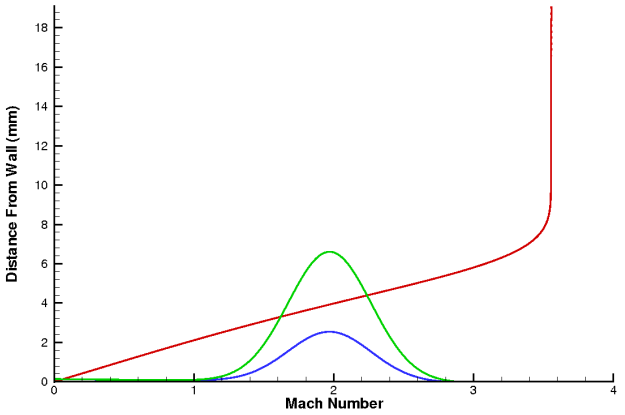

Figure 12. Roughness element heights and Mach profile without roughness. Mach profile without roughness —; Roughness h = 2.54 mm —; Roughness h = 6.60 mm —.

Some non-physical characteristics in the following results should be explained. The pressure contour for the flow with the 2.54 mm roughness element is shown in Fig. 13. There are wiggles seen in the contour lines near the bottom of the Mach wave. These wiggles are mostly localized near the downstream edge of the Mach wave. For both roughness elements, the boundary layer profile is free of oscillations. The oscillations in the Mach wave and expansion fan are due to relatively coarse streamwise resolution far downstream of the roughness element, and can likely be reduced with improved refinement; this will be explored in our ongoing study. There is a weak Mach wave originating at the lower portion of the inlet. The Mach wave is probably caused by the inlet conditions not being able to adjust to the roughness element. A longer upstream portion of the domain is probably required. Since the Mach wave is very weak, it is assumed to not have a substantial effect on the rest of the flow.

V.A. 2.54 mm Roughness Element

Figure 13 clearly shows a Mach wave originating upstream of the roughness element and an expansion wave behind the roughness element. Figure 14 shows a comparison between the boundary layer contours with

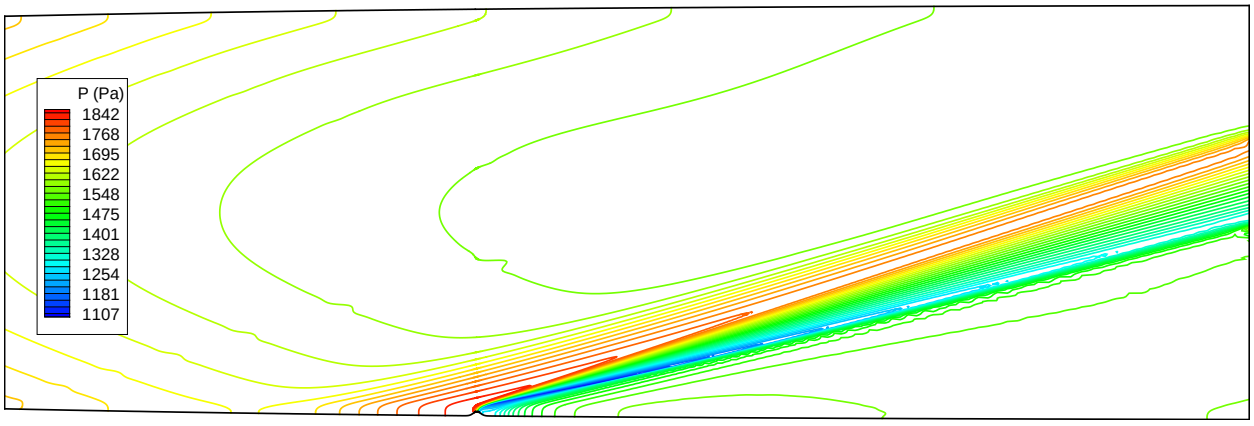

Figure 13. Pressure contour for 2.54 mm roughness element

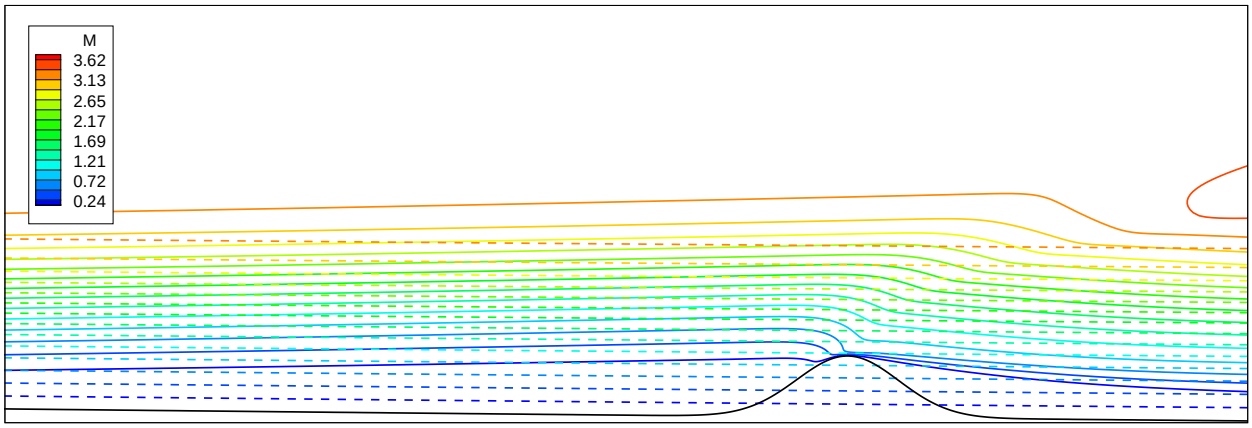

Figure 14. Mach contour for 2.54 mm roughness element. Solid lines are flow with roughness element. Dashed lines are flow without roughness element

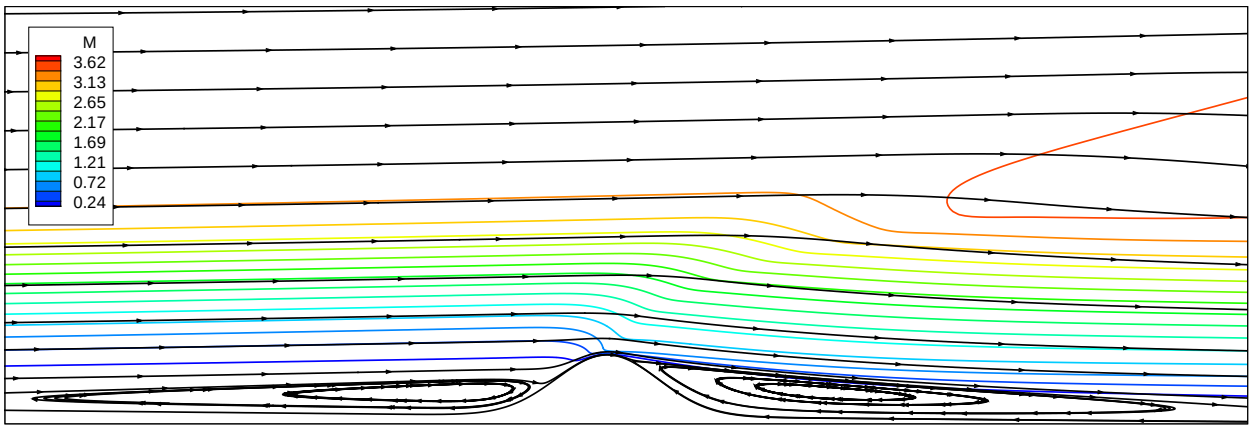

Figure 15. Mach contour with streamlines for 2.54 mm roughness element

and without the roughness element in the vicinity of the roughness elements location. As Fig. 14 shows, the roughness element causes the upstream boundary layer to increase in height, which then acts as a smooth compression corner and produces a Mach wave in the flow. Once the flow travels over the roughness, the flow needs to return to the wall of the nozzle. This makes the downstream portion of the roughness element act as an expansion corner and thus produces an expansion fan originating at the roughness element. The small height of the roughness allows the flow to smoothly adjust to the roughness and thus does not produce any shocks in the nozzle.

Figure 15 shows the Mach contour with streamlines in the vicinity of the roughness element. A recirculation zone is created both upstream and downstream of the roughness element. For this shorter roughness element, the upstream recirculation zone only reaches up about half the height of the roughness element, while the downstream recirculation zone reaches the full height of the roughness element. The flow reattaches approximately 35 mm downstream of the center of the roughness element.

The quantity $\frac{\partial}{\partial y}\left[\rho\frac{\partial U}{\partial y}\right]$ (henceforth referred to as the stability criterion), which is relevant to stability properties of the flow was computed at four locations downstream of the roughness element: approximately 2.024 m , 2.124 m, 2.24 m and 2.324 m downstream of the throat of the nozzle (0.1 m, 0.2 m, 0.3 m and 0.4 m downstream of the roughness element). Figure 16 shows the locations overlaid on the Mach contour. Lees & Lin[22] showed that the existence of a zero in the stability criterion is a necessary condition for inviscid instability in a compressible boundary layer. The plot of the stability criterion along with the U velocity component profile for the four locations is shown in Fig. 17. Only a portion from the lower wall to just outside the boundary layer is shown. All four plots show the roughness element to have only a minimal effect on the

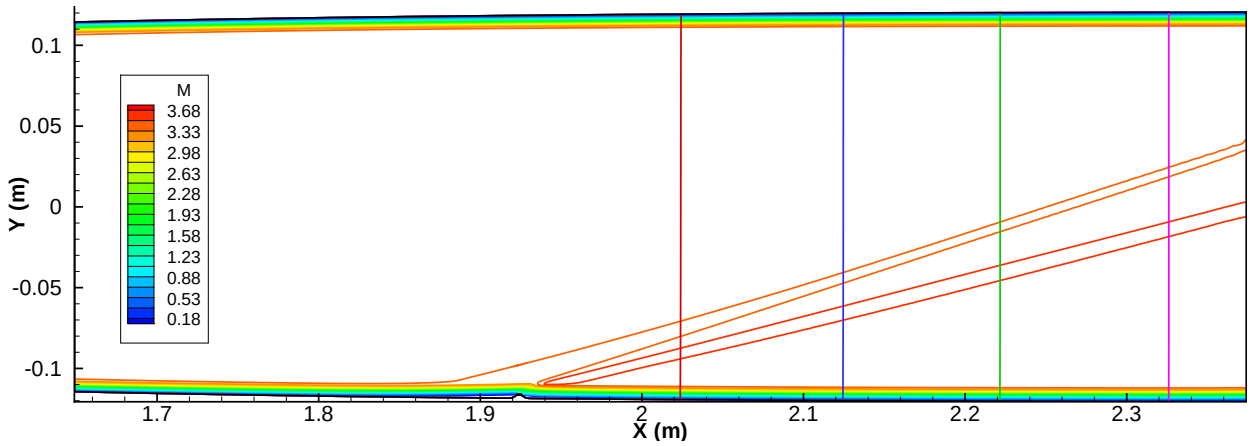

Figure 16. Mach contour with location of stability plots for 2.54 mm roughness element. Location 1 ——; Location 2 ——; Location 3 ——; Location 4 ——.

thickness of the boundary layer. At location 1, the roughness element has the greatest effect on the stability criterion. The roughness element has produced a bump in the profile which creates an addition zero in the stability criterion profile. However, by location 2, the bump has diminished in size greatly and the additional zero is gone. At location 3, aside from small differences in magnitude, there is no discernible differences in the shape of the stability criterion profile from the base flow profile. At location 4, a discrepancy between the stability criterion profile and the base flow profile near the wall appears.

V.B. 6.60 mm Roughness Element

The pressure contour for flow with the 6.60 mm roughness element is shown in Fig. 18. The 6.60 mm roughness element generates a flow field qualitatively similar to the 2.54 mm element. There is again a Mach wave originating upstream of the roughness and an expansion wave downstream the roughness. Although the roughness is approximately 66% of the undisturbed boundary layer thickness, a shock is not created in the nozzle.

The Mach contour with streamlines in the vicinity of the 6.60 mm roughness is shown in Fig. 19. The increase in roughness height has caused the recirculation zone upstream of the roughness element to change. Instead of having one large recirculation zone upstream as in the 2.54 mm roughness element, there are now three distinct zones. The height of the recirculation zone has increased to approximately equal the roughness height. The downstream recirculation zone is still just a single zone whose height is equal to the roughness element. The flow reattaches 93 mm downstream of the roughness element's center. The ratio of the two roughness elements heights is approximately equal to the ratio of their downstream recirculation zones.

The stability criterion was also computed at the same four location for the 6.60 mm roughness element as for the 2.54 mm roughness element. The four locations are depicted in the Mach contour in Fig. 20. The plot of the stability criterion along with the U velocity component profile at the four locations is shown in Fig. 21. As before, only a portion from the lower wall to just outside the boundary layer is plotted. The plots show that the 6.60 mm roughness has much more of an effect then the 2.54 mm roughness element as would be expected. Unlike the 2.54 mm roughness element, the 6.60 mm element has caused a significant change in both the U velocity profile and the stability criterion at location 1. The maximum value near the wall has significantly increased resulting in a much larger distortion of the stability criterion from the base profile. Just as in the 2.54 roughness element, the stability criterion now has an additional zero. The effect of the roughness element at location 2 appears very similar to the effect of the 2.54 mm roughness at location 1 except the stability profile now has one less zero then the base flow. At location 3, the velocity profile is very close to the undisturbed profile and the stability criterion is returning to the undisturbed profile, though is still altered. At location 4, there is no longer any trace of the addition bump in the stability criterion profile that the roughness element produced but there is again the departure from the base flow profile near the wall.

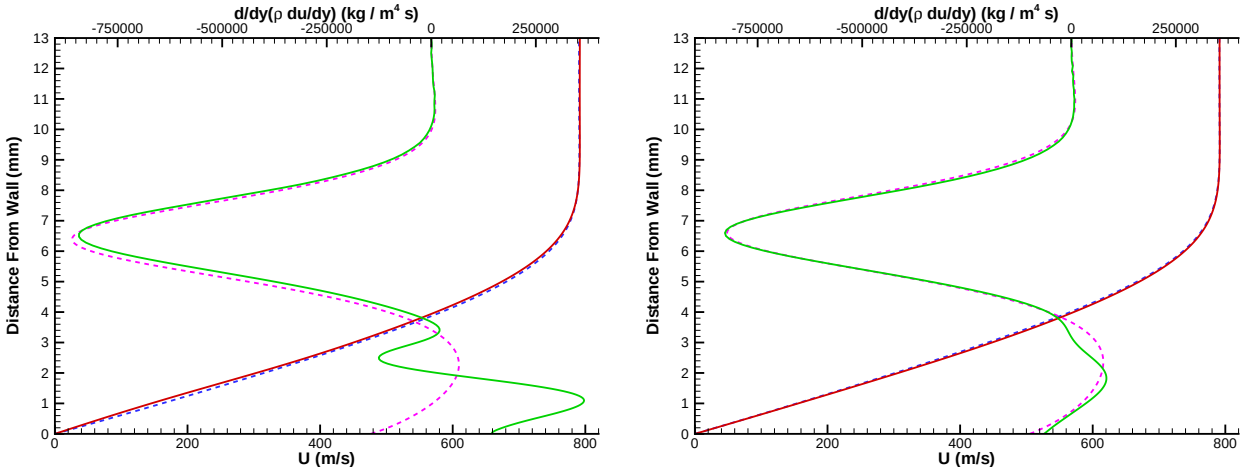

(a) Location 1

(b) Location 2

(c) Location 3

(d) Location 4

Figure 17. Velocity profile with derivative of density times first derivative of velocity for 2.54 mm roughness element. U without roughness - - -; $d/dy(\rho dU/dy)$ without roughness - - -; U with roughness ——; $d/dy(\rho dU/dy)$ with roughness ——.

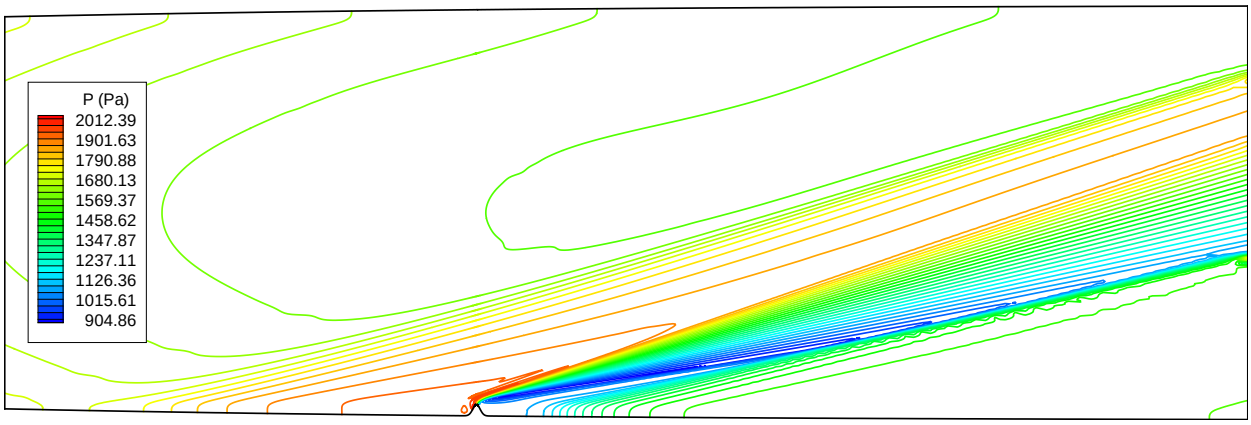

Figure 18. Pressure contour for 6.60 mm roughness element

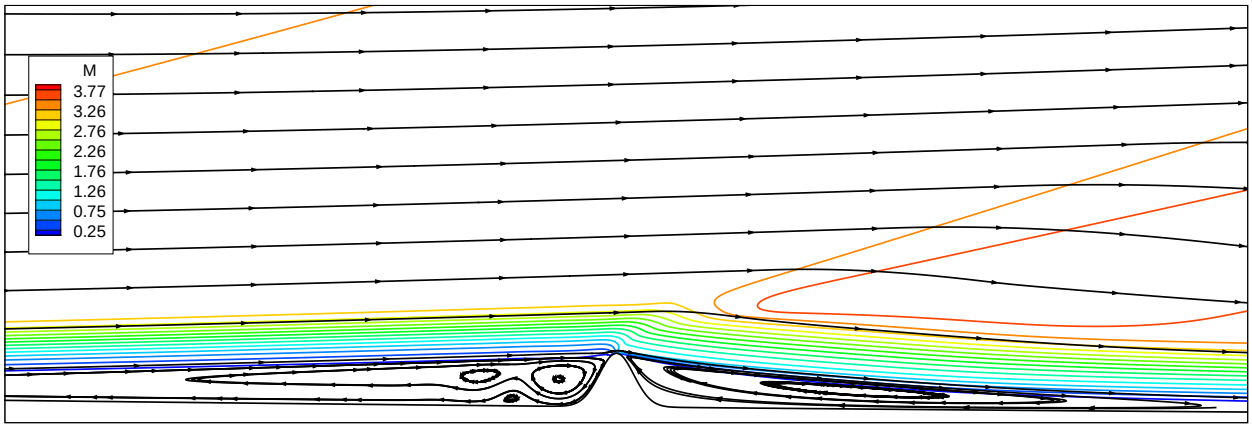

Figure 19. Mach contour with streamlines for 6.60 mm roughness element

VI. Conclusion

This work has used direct numerical simulations to explore the flow generated with and without a finite roughness element on the wall of the Purdue Mach 6 quiet wind tunnel. Three-dimensional simulations for two stagnation pressures were performed and compared with measured results from the Purdue wind tunnel. Good agreement was obtained between the simulation results and the measurements. Two-dimensional simulations were also performed for flow with a 2.54 mm and 6.60 mm roughness element. Both roughness elements produced a combination of Mach wave and expansion fan in the nozzle. A recirculation zone was also produced upstream and downstream of the roughness elements.

Although the general properties of the flow generated by the two roughness elements are the same, the quantitative properties are quiet different. The 6.60 mm roughness effects much more of the flow upstream of the roughness element and thus results in a much thicker Mach wave upstream of the roughness. The flow also has a thicker expansion wave. The increase in roughness height changes the structure of the upstream recirculation zone by generating three recirculation zones instead of one. Increasing the roughness height also increases the length of the downstream recirculation zone. Based on the current results, the increase is linearly proportional to the height of the roughness element. Both roughness elements will generate a bump in the stability criterion which creates an additional zero in the stability criterion profile 0.1 m downstream of the roughness. However, by 0.2 m, the additional zero is gone for the 2.54 mm roughness and the profile is relativity close to the undisturbed profile, while for the 6.60 mm roughness, the stability criterion has one less zero then the undisturbed profile at 0.2 m downstream from the roughness. At 0.3 mm, the stability criterion for the 6.60 mm roughness element is returning to the base flow profile and already has the same number of zeros as the base flow.

In future work, we will extend the simulations of roughness elements to the three-dimensional nozzle and explore the effect of external disturbances on the stability of the flow. We will also abandon the use of a body fitted grid in exchange for the immersed boundary method.

Acknowledgments

The authors gratefully acknowledge support by the NASA Fundamental Aeronautics Program, under cooperative agreement NNX07AC39A, monitored by Dr. Meelan Choudhari. The authors thank Professor Steven Schneider for providing data on the Boeing/AFOSR Mach 6 Wind Tunnel and Mr. Syed Rehman for providing his two-dimensional WENO code used in this research. The authors also thank NASA and TeraGrid for providing computer time to run the numerical simulations.

References

[1]Schneider, S. P., "Hypersonic laminar-turbulent transition on circular cones and scrarajet forebodies," *Progress In Aerospace Sciences*, Vol. 40, No. 1-2, Feb. 2004, pp. 1–50.

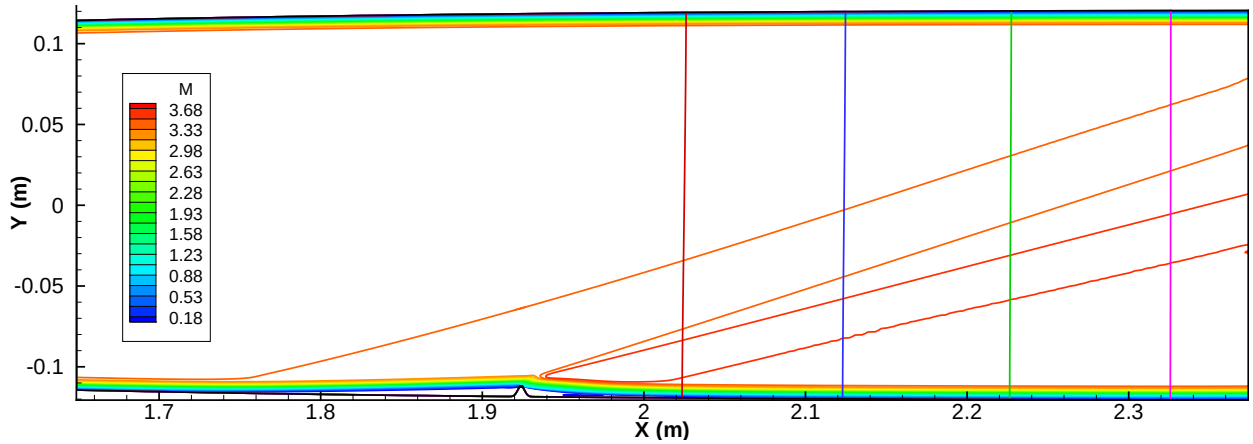

Figure 20. Mach contour with location of stability plots for 6.60 mm roughness element. Location 1 ——; Location 2 ——; Location 3 ——; Location 4 ——.

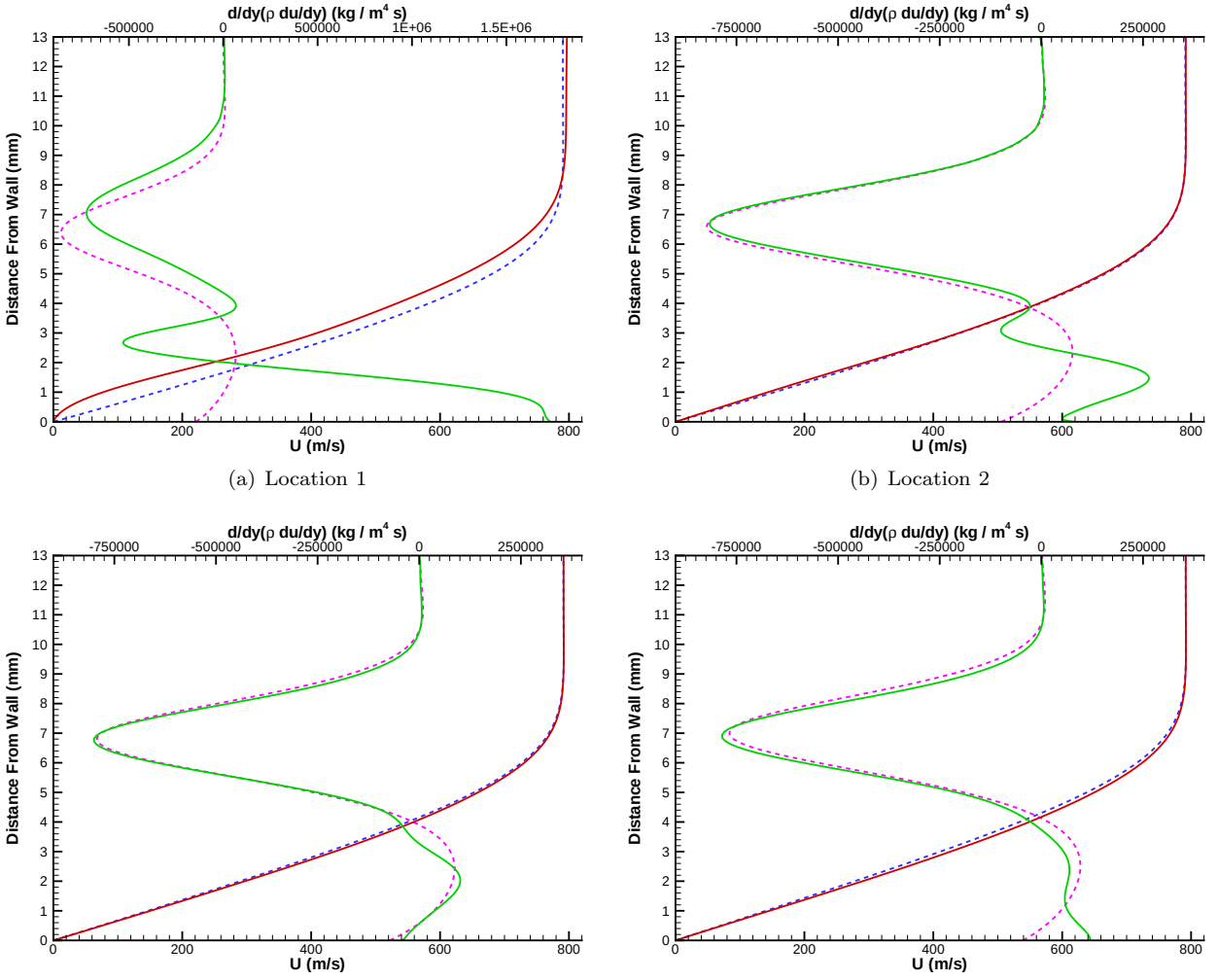

(a) Location 1

(b) Location 2

(c) Location 3

(d) Location 4

Figure 21. Velocity profile with derivative of density times first derivative of velocity for 6.60 mm roughness element. U without roughness - - -; $d/dy(\rho dU/dy)$ without roughness - - -; U with roughness ——; $d/dy(\rho dU/dy)$ with roughness ——.

[2]Schneider, S. P., "Effects of roughness on hypersonic boundary-layer transition," *Journal Of Spacecraft And Rockets*, Vol. 45, No. 2, March 2008, pp. 193–209.

[3]Schneider, S. P., "Hypersonic boundary-layer transition on blunt bodies with roughness," AIAA Paper 2008-501, January 2008.

[4]Hanifi, A., Schmid, P. J., and Henningson, D. S., "Transient growth in compressible boundary layer flow," *Physics Of Fluids*, Vol. 8, No. 3, March 1996, pp. 826–837.

[5]Reshotko, E., "Transient growth: A factor in bypass transition," *Physics Of Fluids*, Vol. 13, No. 5, May 2001, pp. 1067–1075.

[6]Tumin, A. and Reshotko, E., "Spatial theory of optimal disturbances in boundary layers," *Physics Of Fluids*, Vol. 13, No. 7, July 2001, pp. 2097–2104.

[7]Reshotko, E. and Tumin, A., "Role of transient growth in roughness-induced transition," *AIAA Journal*, Vol. 42, No. 4, April 2004, pp. 766–770.

[8]Reda, D. C., "Correlation Of Nosetip Boundary-Layer-Transition Data Measured In Ballistics-Range Experiments," *AIAA Journal*, Vol. 19, No. 3, 1981, pp. 329–339.

[9]Reda, D. C., "Review and synthesis of roughness-dominated transition correlations for reentry applications," *Journal Of Spacecraft And Rockets*, Vol. 39, No. 2, March 2002, pp. 161–167.

[10]White, E. B., "Transient growth of stationary disturbances in a flat plate boundary layer," *Physics Of Fluids*, Vol. 14, No. 12, Dec. 2002, pp. 4429–4439.

[11]White, E. B., Rice, J. M., and Gokhan Ergin, F., "Receptivity of stationary transient disturbances to surface roughness," *Physics Of Fluids*, Vol. 17, No. 6, June 2005, pp. 064109.

[12]Choudhari, M. and Fischer, P., "Roughness-Induced Transient Growth," AIAA Paper 2005-4765, June 2005.

[13]Fischer, P. and Choudhari, M., "Numerical simulation of roughness-induced transient growth in a laminar boundary layer," AIAA Paper 2004-2539, June 2004.

[14]Borg, M., Juliano, T. J., and Schneider, S. P., "Inlet measurements and quiet-flow improvements in the Boeing/AFOSR Mach-6 quiet tunnel," AIAA Paper 2006-1317, January 2006.

[15]Schneider, S. P., "Fabrication and testing of the Purdue Mach-6 quiet-flow Ludwieg tube," AIAA Paper 2000-0295, January 2000.

[16]Zhong, X. L., "High-order finite-difference schemes for numerical simulation of hypersonic boundary-layer transition," *Journal Of Computational Physics*, Vol. 144, No. 2, Aug. 1998, pp. 662–709.

[17]Williamson, J. H., "Low-Storage Runge-Kutta Schemes," *Journal Of Computational Physics*, Vol. 35, No. 1, 1980, pp. 48–56.

[18]Jiang, G. and Shu, C., "Efficient implementation of weighted ENO schemes," *Journal of Computational Physics*, Vol. 126, No. 1, 1996, pp. 202–228.

[19]Spekreijse, S. P., "Elliptic Grid Generation Based On Laplace Equations And Algebraic Transformations," *Journal Of Computational Physics*, Vol. 118, No. 1, April 1995, pp. 38–61.

[20]Thompson, K. W., "Time-Dependent Boundary-Conditions For Hyperbolic Systems," *Journal Of Computational Physics*, Vol. 68, No. 1, Jan. 1987, pp. 1–24.

[21]Skoch, C. R., *Disturbances From Shock/Boundary-Layer Interactions Affecting Upstream Hypersonic Flow*, Ph.D. thesis, Purdue University, December 2005.

[22]Lees, L. and Lin, C., "Investigation of the stability of the laminar boundary layer in a compressible fluid," NACA TN 1115, 1946.